



Seismic velocity structure and depth-dependence of anisotropy in the Red Sea and Arabian shield from surface wave analysis

Samantha E. Hansen,^{1,2,3} James B. Gaherty,⁴ Susan Y. Schwartz,¹ Arthur J. Rodgers,² and Abdullah M. S. Al-Amri⁵

Received 16 August 2007; revised 10 March 2008; accepted 19 March 2008; published 14 October 2008.

[1] We investigate the lithospheric and upper mantle shear wave velocity structure and the depth-dependence of anisotropy along the Red Sea and beneath the Arabian Peninsula using receiver function constraints and phase velocities of surface waves traversing two transects of stations from the Saudi Arabian National Digital Seismic Network. Frequency-dependent phase delays of fundamental-mode Love and Rayleigh waves, measured using a cross-correlation procedure, require very slow shear velocities and the presence of anisotropy to depths of at least 180 km in the upper mantle. Linearized inversion of these data produce path-averaged 1D radially anisotropic models with $\sim 4\%$ anisotropy in the lithosphere and across the lithosphere-asthenosphere boundary (LAB). Models with reasonable crustal velocities in which the mantle lithosphere is isotropic cannot satisfy the data. The lithosphere, which ranges in thickness from about 70 km near the Red Sea coast to about 90 km beneath the Arabian Shield, is underlain by a pronounced low-velocity zone with shear velocities as low as 4.1 km/s. Forward models of azimuthal anisotropy, which are constructed from previously determined shear wave splitting estimates, can reconcile surface and body wave observations of anisotropy. The low shear velocities extend to greater depth than those observed in other continental rift and oceanic ridge environments. The depth extent of these low velocities combined with the sharp velocity contrast across the LAB may indicate the influence of the Afar hot spot and the presence of partial melt beneath Arabia. The anisotropic signature primarily reflects a combination of plate- and density-driven flow associated with rifting processes in the Red Sea.

Citation: Hansen, S. E., J. B. Gaherty, S. Y. Schwartz, A. J. Rodgers, and A. M. S. Al-Amri (2008), Seismic velocity structure and depth-dependence of anisotropy in the Red Sea and Arabian shield from surface wave analysis, *J. Geophys. Res.*, 113, B10307, doi:10.1029/2007JB005335.

1. Introduction

[2] Knowledge of the lithospheric and upper mantle structure beneath the Arabian Peninsula and the Red Sea has important implications for understanding the processes associated with continental rifting. Rifting of the Red Sea began about 30 Ma, separating the western edge of the Arabian Plate from Africa [*Camp and Roobol*, 1992]. Several studies have shown that large-scale extensional stresses initiated rifting in the Red Sea [*Wernicke*, 1985; *Voggenreiter et al.*, 1988; *McGuire and Bohannon*, 1989].

However, more recent work [*Camp and Roobol*, 1992; *Ebinger and Sleep*, 1998; *Daradich et al.*, 2003; *Hansen et al.*, 2006, 2007] has illustrated that within the last 15–20 Ma, lithospheric thinning in the Red Sea has continued as a result of both extension and thermal erosion associated with asthenospheric flow originating from the Afar hot spot (Figure 1).

[3] The Arabian Peninsula is composed of the western Arabian Shield and the eastern Arabian Platform (Figure 1). The Shield is composed of Proterozoic island arc terranes that were accreted together 600–900 Ma, and basement rocks in this region have little to no sediment cover. However, the Proterozoic basement rocks in the Platform are covered by up to 10 km of Phanerozoic sediments [*Stoeser and Camp*, 1985]. Numerous studies have provided details on the crustal and upper mantle structure beneath the Arabian Peninsula. Seismic body and surface wave tomography studies [*Debayle et al.*, 2001; *Benoit et al.*, 2003; *Julià et al.*, 2003; *Nyblade et al.*, 2006; *Tkalčić et al.*, 2006; *Park et al.*, 2007] have shown that the upper mantle beneath the Arabian Shield and the Red Sea is anomalously slow, most likely associated with a broad thermal anomaly, and

¹Earth and Planetary Sciences Department, University of California, Santa Cruz, California, USA.

²Energy and Environment Directorate, Lawrence Livermore National Laboratory, Livermore, California, USA.

³Now at Geosciences Department, Pennsylvania State University, University Park, Pennsylvania, USA.

⁴Lamont-Doherty Earth Observatory, Columbia University, Palisades, New York, USA.

⁵Geology Department and Seismic Studies Center, King Saud University, Riyadh, Saudi Arabia.

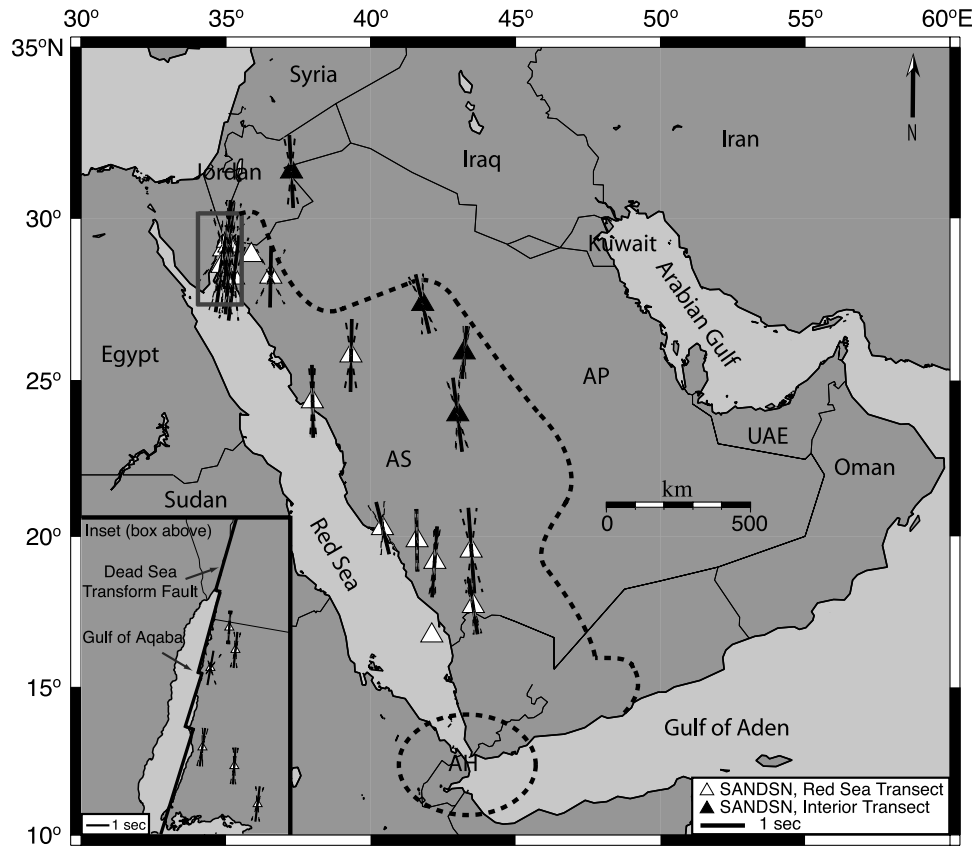


Figure 1. Map showing SANDSN stations from the examined Red Sea transect (white triangles) and interior transect (black triangles). Average splitting parameters, modified from *Hansen et al.* [2006], are overlain on each station. Bold, centerlines are oriented in the station's average ϕ and the length of the line is scaled to the average δt . Dashed “fans” show one standard deviation of ϕ . Inset provides a closer view of the Gulf of Aqaba stations (gray box). Bold, dashed line shows the boundary between the Arabian Shield (AS) and Arabian Platform (AP) while the bold circle (labeled AH) marks the approximate location of the Afar hot spot.

that velocities increase toward the continental interior. Regional waveform modeling [*Rodgers et al.*, 1999] showed that the Arabian Platform has relatively low crustal P- and S-wave velocities ($V_P = 6.07$ km/s, $V_S = 3.50$ km/s) compared to the Arabian Shield ($V_P = 6.42$ km/s, $V_S = 3.70$ km/s). However, below the Moho, seismic velocities in the Shield ($V_P = 7.90$ km/s, $V_S = 4.30$ km/s) are slower than in the Platform ($V_P = 8.10$ km/s, $V_S = 4.55$ km/s). P- and S-wave receiver functions reveal a shallow Moho (~ 20 km) and lithosphere-asthenosphere boundary (LAB, ~ 60 km) along the Red Sea coast, both of which become deeper toward the Arabian interior [*Sandvol et al.*, 1998; *Al-Damegh et al.*, 2005; *Hansen et al.*, 2007]. Crustal thickness reaches a maximum of 40–45 km beneath the central Arabian Shield and Platform. The lithospheric thickness is about 120 km beneath the central Arabian Shield; however, at the Shield-Platform boundary the lithospheric thickness increases to about 160 km. At most examined stations, a pronounced low-velocity zone (LVZ) underlies the lithospheric lid, and the LAB is associated with an approximate 6% V_S decrease [*Tkalčić et al.*, 2006; *Hansen et al.*, 2007].

[4] Upper mantle anisotropy beneath the Arabian Peninsula has also been explored using teleseismic shear wave splitting [*Wolfe et al.*, 1999; *Hansen et al.*, 2006]. This

anisotropy most likely arises from the lattice-preferred orientation (LPO) in peridotite rocks, where the fast axis (ϕ) corresponds to the olivine crystallographic a-axes [100] and the delay time (δt) represents the shear velocity difference integrated over depth [e.g., *Silver*, 1996]. Most of the splitting observations across Arabia show a very consistent pattern, with a north-south oriented ϕ and δt averaging about 1.4 s (Figure 1). *Hansen et al.* [2006] concluded that the anisotropy reflects combined plate- and density-driven flow in the asthenosphere. While the lithosphere, especially near the Red Sea coast, is not thick enough to generate the observed δt , a lithospheric component cannot be completely ruled out as the Proterozoic terranes composing the Arabian Shield mainly strike north-south. Therefore some of the observed splitting might be attributed to fossilized structure associated with the assembly of the Shield. Fairly good back-azimuth coverage was obtained with the examined phases, with the largest azimuthal gap between 115° – 210° . No evidence for multiple anisotropic layers was observed [*Hansen et al.*, 2006] so if anisotropy is present in both the lithosphere and asthenosphere, the ϕ in both regions must be similar.

[5] In this paper, we further characterize the lithospheric and upper mantle structure as well as the anisotropy along

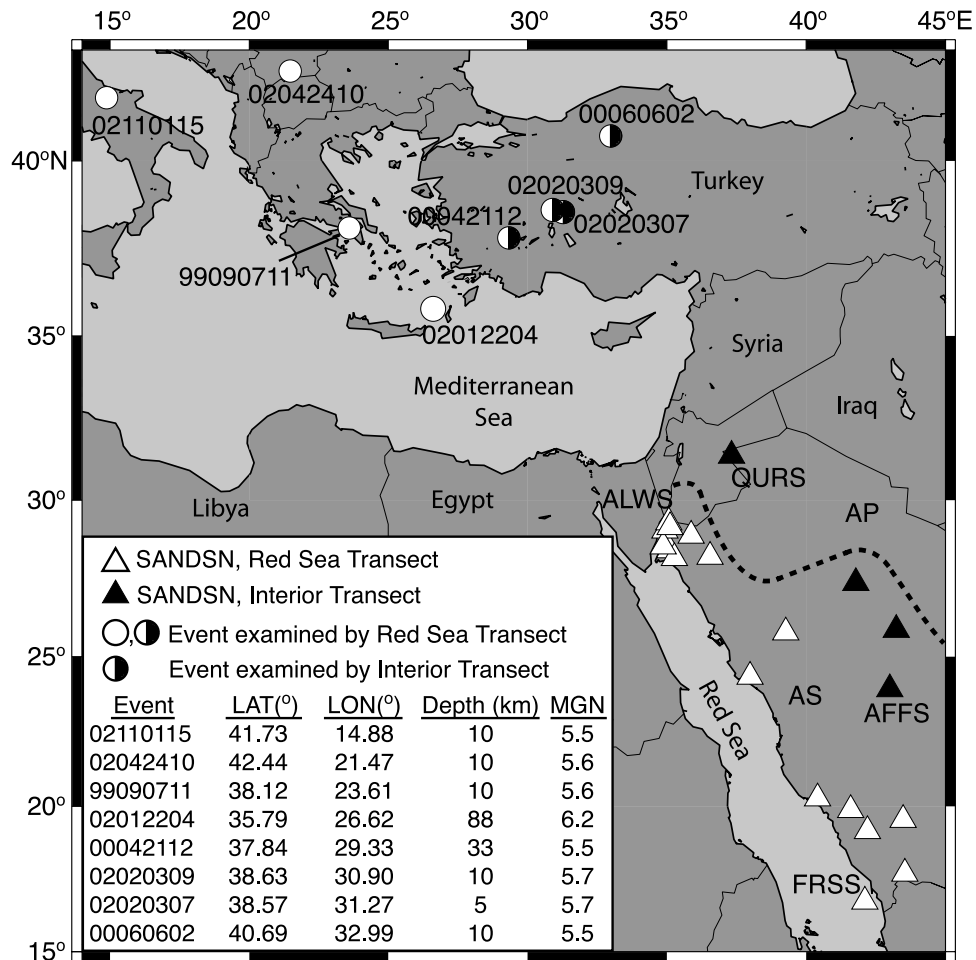


Figure 2. Map showing SANDSN stations from the Red Sea transect (white triangles) and interior transect (black triangles) along with the eight regional earthquakes used in this study. All eight earthquakes (circles) were examined at stations in the Red Sea transect, but only the four most eastern earthquakes (half black, half white circles) were examined at stations in the interior transect. Bold, dashed line shows the boundary between the Arabian Shield (AS) and Arabian Platform (AP). Names of the first and last stations along each transect are listed as are the earthquake IDs. Additional information about these earthquakes is provided in the legend.

the Red Sea and beneath the Arabian Peninsula by jointly inverting surface wave delay times and receiver function constraints. Fundamental-mode surface wave observations are sensitive to vertical velocity averages while receiver functions are sensitive to velocity contrasts and vertical traveltimes [Julia *et al.*, 2003]. Combining their complementary information provides tighter constraints on the shear wave velocity structure. Discrepancies between the Love and Rayleigh wave velocities at different frequencies also allow us to determine the depth distribution of radial anisotropy. We apply this approach to eight regional earthquakes which produced surface waves that traversed two distinct transects along the Red Sea and interior Arabian Peninsula. Phase delays of Love and Rayleigh waves from these events, along with Moho and LAB-generated S-P times from S-wave receiver functions [Hansen *et al.*, 2007], are inverted to evaluate the depth-dependent seismic velocity and anisotropy structure beneath these two transects. Additionally, forward models of azimuthal anisotropy are examined to evaluate whether estimates derived from shear wave

splitting can also satisfy the surface wave data. Our inversion results demonstrate that the lithospheric lid along each transect is underlain by a pronounced LVZ, with V_S as low as 4.1 km/s, and that anisotropy is required in both the lithosphere and asthenosphere. Forward models can reconcile surface and body wave observations of anisotropy and support the conclusions of Hansen *et al.* [2006] that anisotropy is dominantly controlled by flow in the asthenosphere.

2. Surface Wave Traveltimes

[6] We analyze surface-wave traveltimes from eight moderate-sized earthquakes which occurred to the northwest of Arabia (Figure 2). These events ranged in magnitude from 5.5 to 6.2. Three-component seismograms were recorded by stations of the Saudi Arabian National Digital Seismic Network (SANDSN [Al-Amri and Al-Amri, 1999]). For this study, we focus on two transects of SANDSN stations. The first transect includes 16 stations covering approximately a 250 km wide span adjacent to the Red Sea, while the second

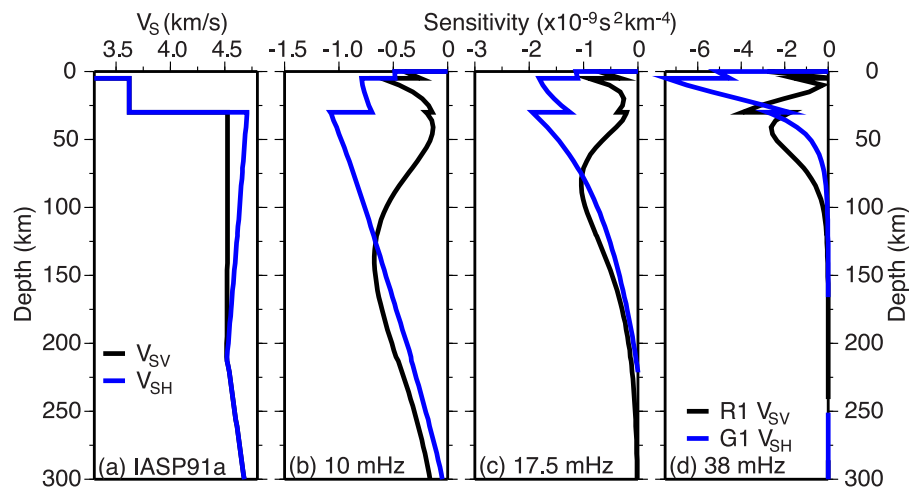


Figure 3. (a) Reference shear velocity model IASP91a, with V_{SH} shown in blue and V_{SV} shown in black. (b-d) Representative partial derivative kernels for fundamental-mode Rayleigh (black) and Love (blue) phase delays as a function of depth for three different frequencies. Reference model for all kernels is IASP91a; kernels shown all correspond to observations from event 00042112 at a station near the front-end of the Red Sea transect. The kernels are with respect to the most sensitive model parameter for each wave type, i.e., the Rayleigh wave kernel is for V_{SV} and the Love wave kernel is for V_{SH} . These kernels give a feel for the depth sensitivity of the phase-delay observations at different frequencies, with higher frequencies sensitive to the shallower depths. Rayleigh waves sample deeper than Love waves at the same frequency. The kernels are negative because an increase in velocity leads to a decrease in phase delay [Gaherty *et al.*, 1996]. (b) Kernels for observations with center frequency of 10 mHz, which are sensitive well into the asthenosphere. (c) Kernels for 17.5 mHz observations, which are sensitive primarily to the upper asthenosphere. (d) Kernels for 38 mHz, which are most sensitive to crustal structure.

transect includes 4 stations located further inland on the Arabian Peninsula (Figures 1 and 2). All eight events were examined at stations along the Red Sea transect since these events and stations share a fairly common great circle path. However, seismograms for only the four most eastern events were examined at stations along the interior transect since the remaining events were further off this transect's great circle orientation (Figure 2). The seismograms were rotated into the receiver-source coordinate system and band-pass filtered between 5 and 50 mHz. In general, the SANDSN data are of excellent quality and all events produced high signal-to-noise (S/N) ratio surface waves in this band. Full synthetic seismograms were also calculated for all eight events at a center frequency of 35 mHz using a normal-mode technique and a modified version of the IASP91 Earth model [Kennett and Engdahl, 1991], assuming mechanisms obtained from the Global CMT catalogue. The synthetics were convolved with the appropriate instrument responses and filtered like the data.

[7] Frequency-dependent traveltimes were measured using a cross-correlation procedure [Gee and Jordan, 1992; Gaherty *et al.*, 1996; Gaherty, 2004]. This method uses a synthetic target wave group (in this case, synthetic fundamental mode surface waves) to estimate phase delays of the observed arrival relative to the synthetic as a function of frequency. The synthetic wave group, called an isolation filter, is cross-correlated with both the data and the full synthetic seismograms. The resulting cross-correlograms are then windowed and narrow-band filtered at discrete frequency intervals (10, 12.5, 15, 17.5, 20, 25, 30, and

38 mHz), and the phase of each correlogram is estimated at each frequency. Phase delays are determined by subtracting each synthetic-isolation-filter phase from the corresponding data-isolation-filter phase, which helps to minimize any potential bias associated with windowing and filtering. Again, the synthetic seismograms and therefore the phase delay measurements were made using the IASP91a model (Figure 3), in which radial anisotropy in the upper 200 km has been added to the isotropic IASP91 structure [Kennett and Engdahl, 1991]. Sensitivity kernels associated with each phase delay were also calculated. These kernels are specific to each observation and account for interference from unmodeled phases [Gaherty *et al.*, 1996]. This analysis was applied to all Love and Rayleigh wave data and each observation provides sensitivity to the path-averaged crustal and mantle structure. Generally, the two highest frequencies are dominated by the crustal structure, the 15–25 mHz bands are sensitive to the mantle lithosphere and upper asthenosphere, and the lowest frequencies provide sensitivity in the asthenosphere down to a depth of about 300 km (Figure 3).

[8] Phase delays relative to IASP91a along the Red Sea transect are shown by the open symbols in Figures 4 and 5, while phase delays along the interior transect are shown in Figures 6 and 7. In all cases, the times are grouped by center frequency and are plotted as a function of distance along the respective transect. For the Red Sea transect, a distance of zero corresponds to station ALWS and the largest distance near 14° corresponds to station FRSS (Figures 2 and 4–5). Similarly, on the interior transect, a distance of zero corre-

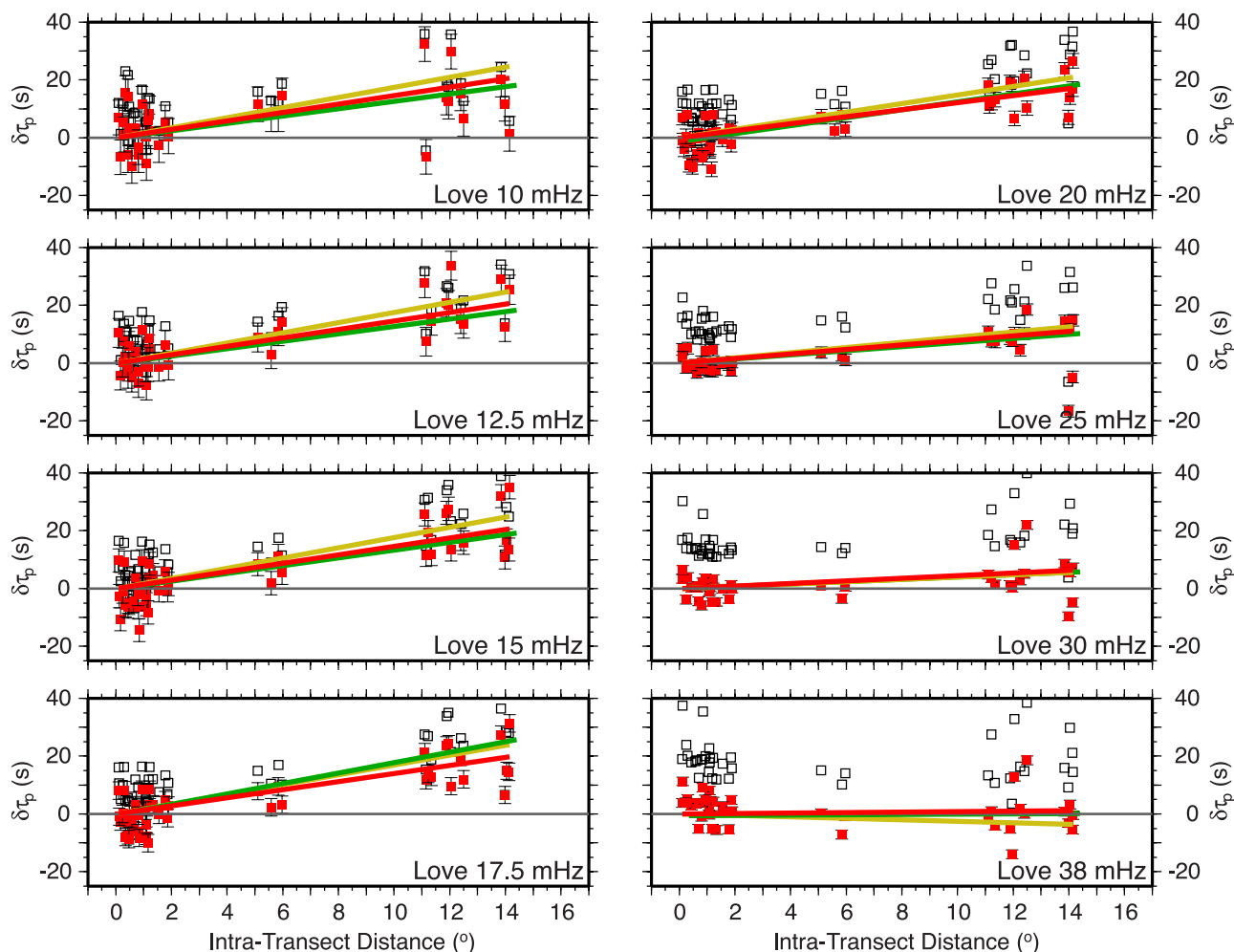


Figure 4. Frequency-dependent phase delays (travel times) of all observed fundamental mode Love waves relative to IASP91a, plotted as a function of distance along the Red Sea transect. Open symbols represent raw observations from each event while solid, red symbols represent the data after they have been corrected for structure outside the transect by subtracting the delay that accumulates between each event and the first station, using the P1 path model shown in Figure 8. Error bars represent a priori estimates based on S/N ratio and frequency. Horizontal line marks a phase delay of zero. Bold red and gold lines show the fit of preferred subarray models RS and RSw in Figure 9, respectively. Bold green lines show the fit of model RS when this model is forced to return to IASP91a at 180 km depth. Note the variation at lower frequencies. Each panel presents observations at a specified frequency, ranging from 10 to 38 mHz.

sponds to station QURS and the largest distance near 9° corresponds to station AFFS (Figures 2 and 6–7). A positive phase delay indicates that the observation is late relative to the arrival time predicted by the synthetic data. Several important observations are worth mentioning. First, there is a fair amount of scatter in the data, especially along the Red Sea transect, and this scatter tends to be somewhat more substantial at lower frequencies. Much of the scatter is probably due to the fact that the earthquakes and stations do not lie on exactly the same great circle path. Additionally, scatter likely results from lower S/N ratios at lower frequencies from the moderate-sized events examined. Yet, despite the data scatter, the Love and Rayleigh wave delay times show a clear increase with increasing distance in most frequency bands, indicating that the velocities below the examined stations are much slower than those of the reference model. The interior transect (Figures 6 and 7)

includes fewer observations, but smaller phase delay trends along this transect indicate faster velocities in the Arabian interior relative to the Red Sea.

[9] To model the phase delay observations, an array-based analysis scheme is employed [Freybourger *et al.*, 2001]. In this approach, the delay time at the first station along each examined transect is sensitive to the source location, origin time, initial phase, and structure outside the array of stations, while variations in delay time along the transect reflect structure beneath it. It is assumed that the individual source-receiver paths travel a similar great circle azimuth, which is not strictly true for the examined events. Raypaths from the events to a common station are furthest apart near the source, but there is still some variation once the station is reached. While this spread leads to a fair amount of data scatter along each transect (Figures 4–7), clear phase delay trends are still readily observed in all

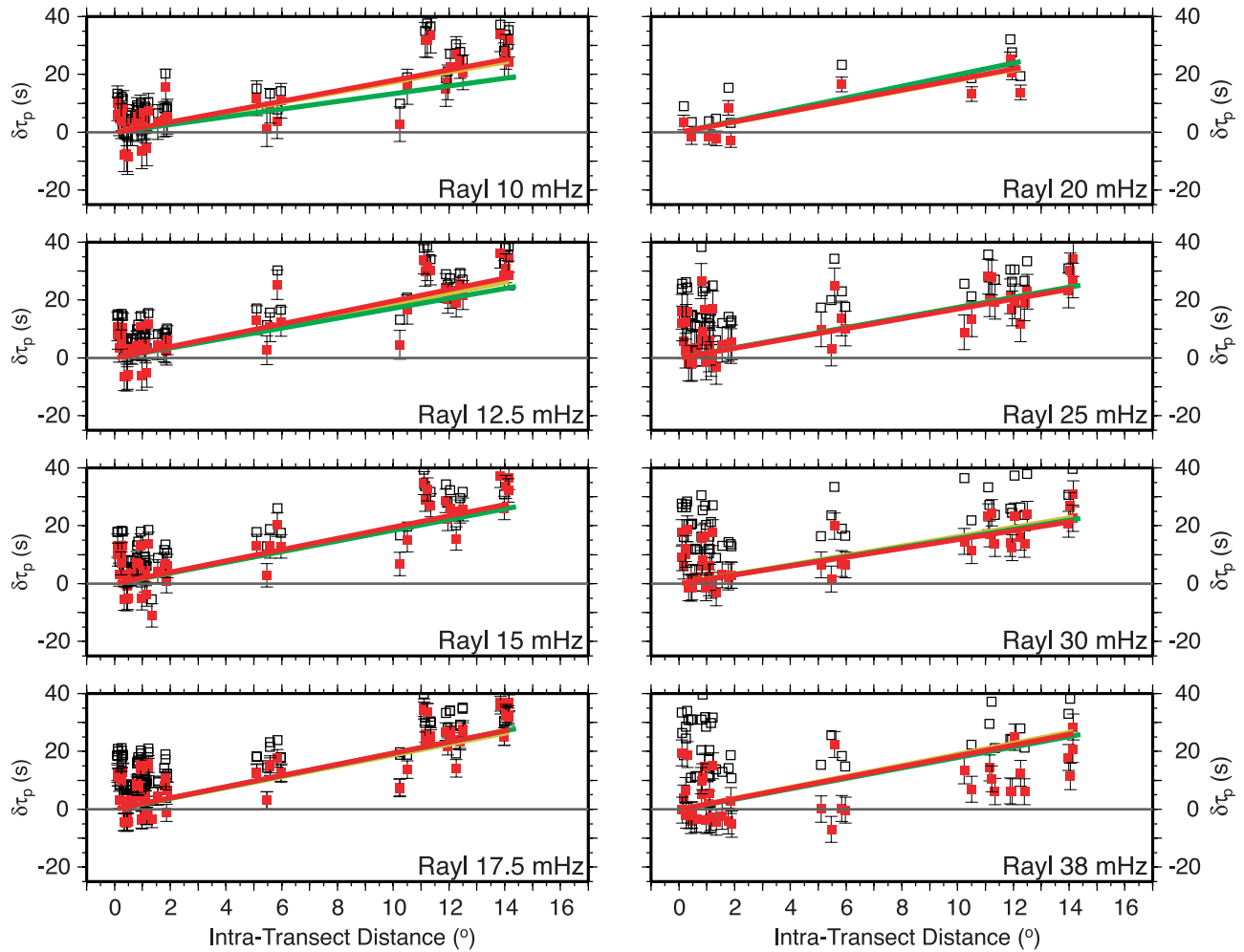


Figure 5. Same as Figure 4, but for fundamental-mode Rayleigh waves. Note the misfit to the lower frequencies when model RS is forced to return to IASP91a at 180 km depth (bold green lines). This indicates that the LVZ beneath the Red Sea transect must extend to depths greater than 180 km.

frequency bands. Therefore the geometry was accepted as being close enough for an array-based approach.

[10] Two structural regimes were established for each examined transect. The structure between the events and the first station in each transect is characterized by an average path model. The phase delays across each transect (from the first to the last station) characterize the average subarray structure. Modeling of the subarray structure takes two forms. First, the phase-delay observations along each transect are inverted for radially anisotropic models of the upper mantle. Then, azimuthally anisotropic models are constructed based on the shear wave splitting results of Hansen *et al.* [2006] and on estimates of intrinsic peridotite elasticity. Using the sensitivity kernels for the observations, forward modeling is used to evaluate whether the splitting-derived models can also satisfy the surface wave data. These different modeling approaches will be described in detail in the following sections.

3. Inverse Models of Radial Anisotropy

[11] The phase delay data are inverted for 1D path-averaged models of radial anisotropy using a linearized

least squares method [Freybourger *et al.*, 2001]. Radial anisotropy represents the simplest parameterization that can satisfy the Love-Rayleigh discrepancy [e.g., Dziewonski and Anderson, 1981; Gaherty *et al.*, 1999]. While these models are transversely isotropic and cannot explain the shear wave splitting data, they provide a way to quantify the depth distribution of the anisotropic structure affecting the surface waves and the relationship of this structure to discontinuities and features of the mantle [Gaherty *et al.*, 1999]. The difference between the actual anisotropy and the radial average depends on the orientation of olivine alignment relative to the propagation direction along the examined corridors. For the two transects examined in this study, the LPO direction, inferred from shear wave splitting [Hansen *et al.*, 2006], is oblique to the propagation direction. With this orientation, the path-averaged radial anisotropy derived from the inversion will be similar to the azimuthal average of the local anisotropy along each examined transect [Maupin, 1985].

[12] Each transect was inverted separately and the corresponding model space contains two structural regions. For the Red Sea transect, the phase delays are modeled by both a path model (P1), which describes the average

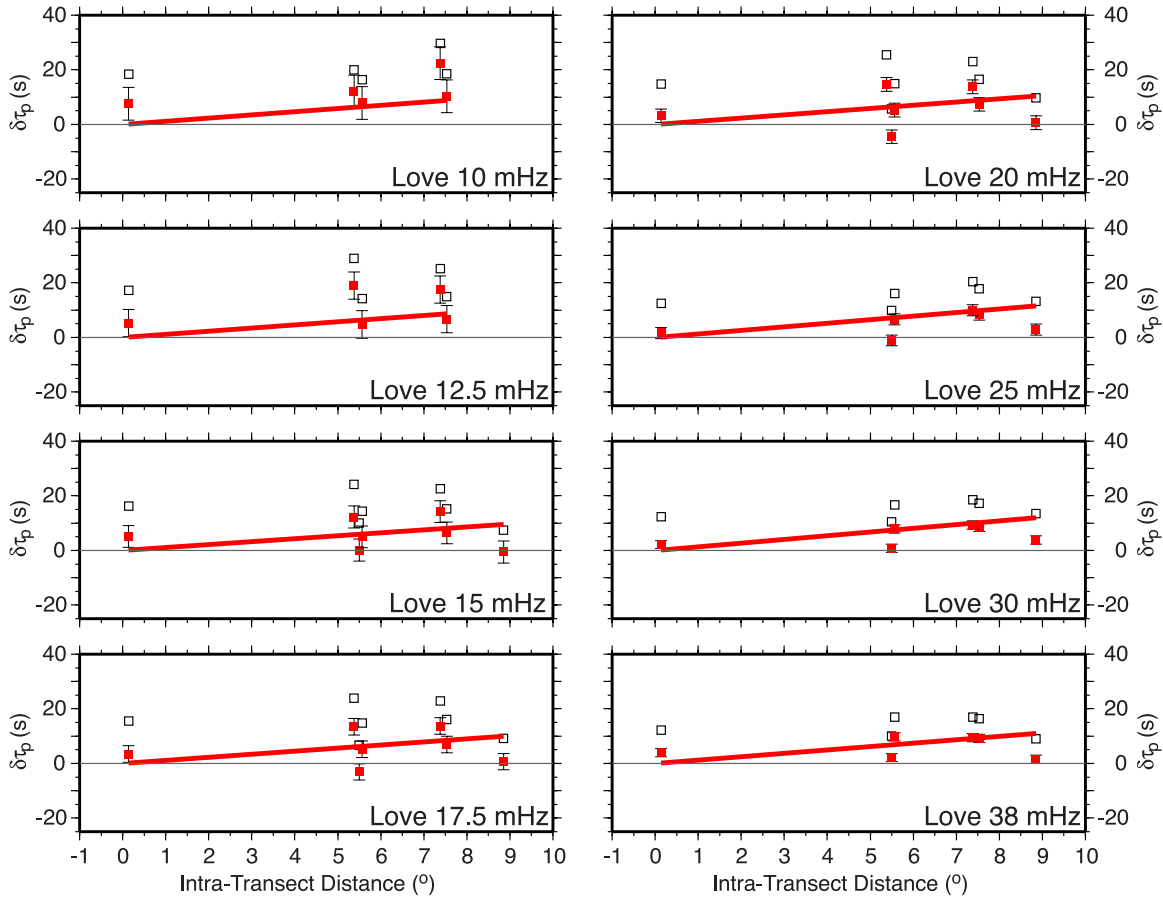


Figure 6. Frequency-dependent phase delays (travel times) of all observed fundamental mode Love waves relative to IASP91a, plotted as a function of distance along the interior transect. Open symbols represent raw observations from each event while solid, red symbols represent the data after they have been corrected for structure outside the transect by subtracting the delay that accumulates between each event and the first station, using the P2 path model shown in Figure 8. Error bars represent a priori estimates based on S/N ratio and frequency. Horizontal line marks a phase delay of zero and bold, red line shows the fit of preferred subarray model INT in Figure 9. Each panel presents observations at a specified frequency, ranging from 10 to 38 mHz.

structure between the events and station ALWS, and a subarray model (RS), which describes the average structure between stations ALWS and FRSS. For the interior transect, the path model (P2) describes the average structure between the events and station QURS while the subarray model (INT) describes the average structure between stations QURS and AFFS. The models consist of five parameters of radial anisotropy (V_{PH} , V_{PV} , V_{SH} , V_{SV} , and η [e.g., *Dziewonski and Anderson, 1981*]), but since the surface wave data are most sensitive to V_{SV} and V_{SH} , we will focus on these parameters. The structures for each transect (P1, RS, P2, and INT) are nominally independent, but nearly identical model and damping parameters ensure similarity.

[13] For each transect, a suite of models that fit the data equally well were found. Therefore a hypothesis testing approach was used to evaluate the characteristics of these models that are necessary to fit the data [*Gaherty and Jordan, 1995; Gaherty et al., 1996; Gaherty, 2004*]. Different distributions of seismic anisotropy were considered and the following hypotheses were tested for each transect.

[14] 1. The entire upper mantle (down to 300 km depth) is isotropic (with $V_{PH} = V_{PV}$, $V_{SH} = V_{SV}$, $\eta = 1$).

[15] 2. The anisotropy is concentrated between the Moho and the LAB (i.e., the lithosphere is anisotropic while the asthenosphere is isotropic).

[16] 3. The anisotropy is concentrated below the LAB (i.e., the asthenosphere is anisotropic while the lithosphere is isotropic).

[17] 4. Anisotropy is required throughout the entire upper mantle (i.e., both the lithosphere and asthenosphere are anisotropic).

[18] S-P vertical traveltimes to the Moho and LAB, determined by S-wave receiver functions [*Hansen et al., 2007*], were also used in the inversions to provide additional constraints on the lithospheric structure beneath each transect. Since receiver functions are primarily sensitive to velocity contrasts and vertical traveltimes while surface wave observations are sensitive to vertical velocity averages, their combination helps to remove resolution gaps associated with each data set and results in models that are

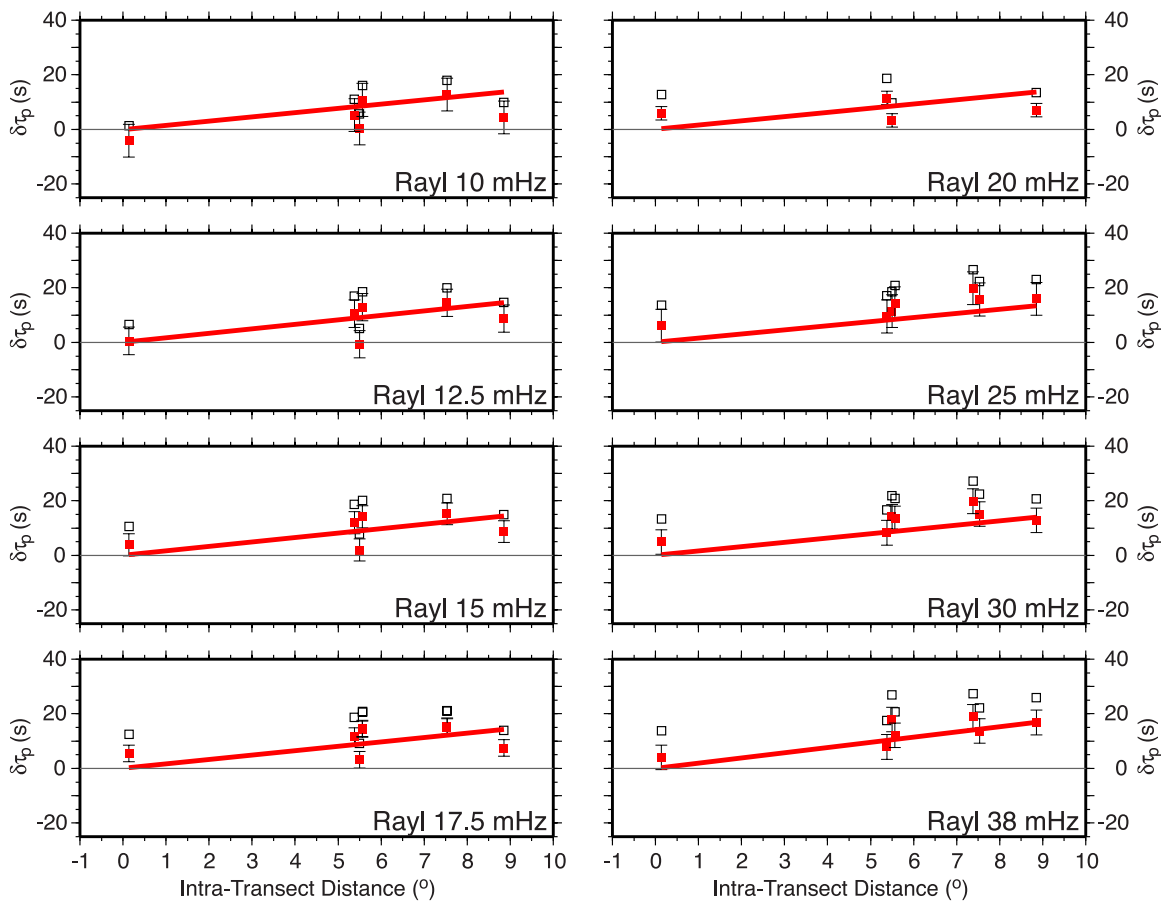


Figure 7. Same as Figure 6, but for fundamental-mode Rayleigh waves.

consistent with both types of observations [Gaherty *et al.*, 1999; Julià *et al.*, 2003]. The receiver function data provide a layered framework for the model space while the surface waves constrain the velocity in that space, thereby reducing the tradeoffs between depth and velocity. From the S-wave receiver functions, stations along the Red Sea displayed average S-P times to the Moho and LAB of 4.22 and 8.57 s, respectively. Using assumed velocities, it was found that these times correspond to average depths of 31 and 65 km. Similarly, stations along the interior transect displayed Moho and LAB S-P times of 4.86 and 10.5 s, respectively, corresponding to average depths of 36 and 80 km [Hansen *et al.*, 2007]. Inverting these S-P times with the well-constrained velocities provided by the surface wave observations allows for more accurate determination of the seismic structure than either data set alone can provide.

[19] The hypothesis tests were performed independently for each region of the model space (P1, RS, P2, and INT). In all cases, goodness of fit was evaluated from formal estimates of normalized chi-square, variance reduction, and S-P time residuals as well as by visual inspection of the fit to the along-transect trends in phase delay, which is not necessarily captured by formal misfit estimates based on individual delay times. The preferred models explain over 90 percent of the variance along both transects relative to the reference model, and all S-P residuals are less than 0.5 s, which is well within the errors of the S-wave receiver function measurements.

[20] The preferred path models are shown in Figure 8. P1 represents the average structure across the eastern Mediterranean, between the events and station ALWS (Figure 2). It is characterized by a 38 km thick crust and upper mantle velocities that are slightly slower than the reference model. Radial anisotropy is at a maximum ($\sim 4.4\%$) just below the Moho and decreases with depth. Although the area incorporated by this path model has been shown to display significant crustal thickness and velocity variations, the average values presented here are similar to the average values observed in previous studies [e.g., Di Luccio and Pasyanos, 2007]. P2 represents the average structure primarily across central Turkey, the eastern edge of the Mediterranean, and western Syria (Figure 2). This model has a somewhat thinner crust than the P1 model and much slower upper mantle velocities. Only a small percentage of radial anisotropy ($\sim 2\%$) is required in the upper 80 km. However, it is important to note that the P2 model is critically constrained by event 00060602 recorded at station QURS (Figure 2). Any potential source errors associated with this event's location or origin time will dramatically affect the models associated with the interior transect; therefore the results obtained along the interior profile are not nearly as robust as those obtained along the Red Sea profile. This may also explain why the P2 model is so much slower than P1, though very low shear velocities beneath Turkey and western Syria have been observed in previous studies, perhaps associated with a thin, hot lithospheric

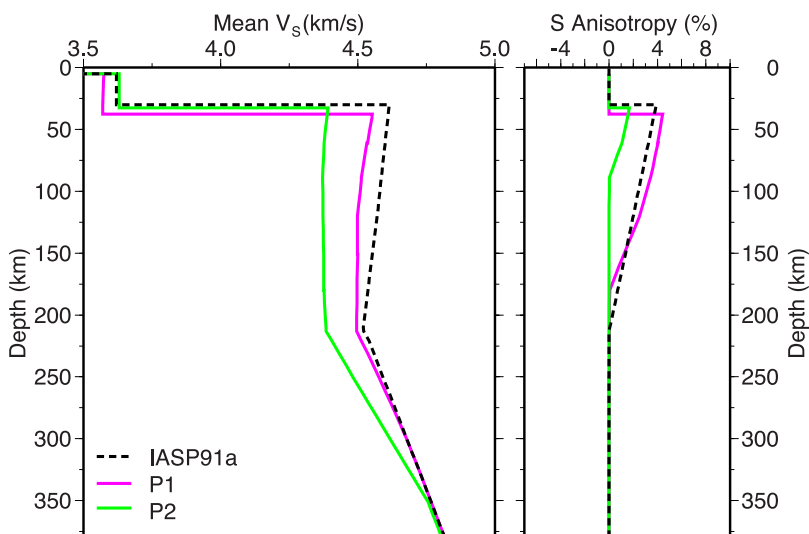


Figure 8. Radially anisotropic shear velocity structure of path models P1 (pink curves) and P2 (green curves). Also shown is the reference model IASP91a (black dashed curves). Left panel displays mean shear velocity ($V_S = (V_{SH} + V_{SV})/2$), while right panel displays shear anisotropy ($\Delta V_S = (V_{SH} - V_{SV})/V_S$ in percent).

mantle [Gök et al., 2003; Di Luccio and Pasyanos, 2007; Gök et al., 2007]. The solid symbols in Figures 4–7 show the traveltimes data across the array corrected for the appropriate path model (P1 or P2). If these path model corrections were perfect, the data would have a zero-second delay time at zero distance. Despite the data scatter on the Red Sea transect (Figures 4 and 5), the P1 model results in an average phase delay of 0 s for stations near zero distance across all Love and Rayleigh wave frequency bands. Again, for the interior transect (Figures 6 and 7), the path corrections greatly depend on any measurement and source errors associated with the one event constraining the P2 model.

[21] Figure 9 displays the mean shear velocity and shear anisotropy for the preferred subarray transect models, and the solid red lines on Figures 4–7 show the average fit of these models to the corresponding path-corrected phase delay data. Also shown on Figures 4, 5, and 9a is model RSsw, which is the preferred subarray model for the Red Sea transect that was obtained only using the surface wave delay times (without including the S-P constraints from the S-wave receiver functions in the inversion). RS is characterized by a 31 km thick crust with average crustal and lithospheric mantle V_S of 3.74 and 4.42 km/s, respectively. The LAB, which is located at a depth of 72 km, is marked by a dramatic V_S decrease, where the average V_S drops to about 4.1 km/s (Figure 9a). These boundary depths and velocities agree well with previous estimates obtained from waveform modeling and receiver functions [Rodgers et al., 1999; Al-Damegh et al., 2005; Hansen et al., 2007]. In addition, by comparing models RS and RSsw, it is clear that the low V_S values observed in the LVZ are not artifacts of the lid structure imposed by the receiver function constraints. Tradeoffs between the crustal velocities and thicknesses as well as the lithospheric velocities in these two models lead to an average fit of the path-corrected phase delay data along the Red Sea transect that is almost identical (Figures 4–5). The surface wave observations alone cannot

resolve the thin lithospheric lid; therefore, the approach of combining the complimentary surface wave and receiver function data better resolves the associated structure and the large velocity contrast associated with the LAB.

[22] The interior model (INT) is characterized by a 37 km thick crust with average crustal and lithospheric mantle V_S of 3.65 and 4.47 km/s, respectively. The LAB along this transect is located at a depth of 92 km and is again associated with a dramatic V_S decrease, down to about 4.2 km/s (Figure 9b). Given the uncertainty with the associated path model (P2) and the limited number of surface wave observations included in the inversion, care must be taken in the interpretation of the INT model. Generally, the boundary depths obtained agree well with those determined from P- and S-wave receiver functions [Al-Damegh et al., 2005; Hansen et al., 2007] and support a thickening of both the crust and lithosphere toward the Arabian interior.

[23] The subarray models display positive ($V_{SH} > V_{SV}$) shear anisotropy below the Moho with slight increases in the anisotropy at the LAB (Figure 9). On the more robust RS model, we observe 3.7% anisotropy in the lithosphere, increasing to 4.6% across the LAB. The anisotropy gradually decays with depth, and the model becomes isotropic by about 200 km. The lithospheric anisotropy is a necessity. Alternative models in which the entire upper mantle is isotropic or in which the anisotropy is concentrated in the asthenosphere push the crustal and upper mantle velocities to unreasonable values and therefore are rejected. The data fit is also improved by including anisotropy in the asthenosphere, but the maximum depth to which anisotropy extends is poorly constrained. The anisotropy could terminate as shallow as ~ 120 km, but it may continue throughout the upper mantle.

[24] The range of models that fit the data equally well provides rough bounds on the model errors (Figure 9). For the Red Sea transect, the mean shear velocities are estimated

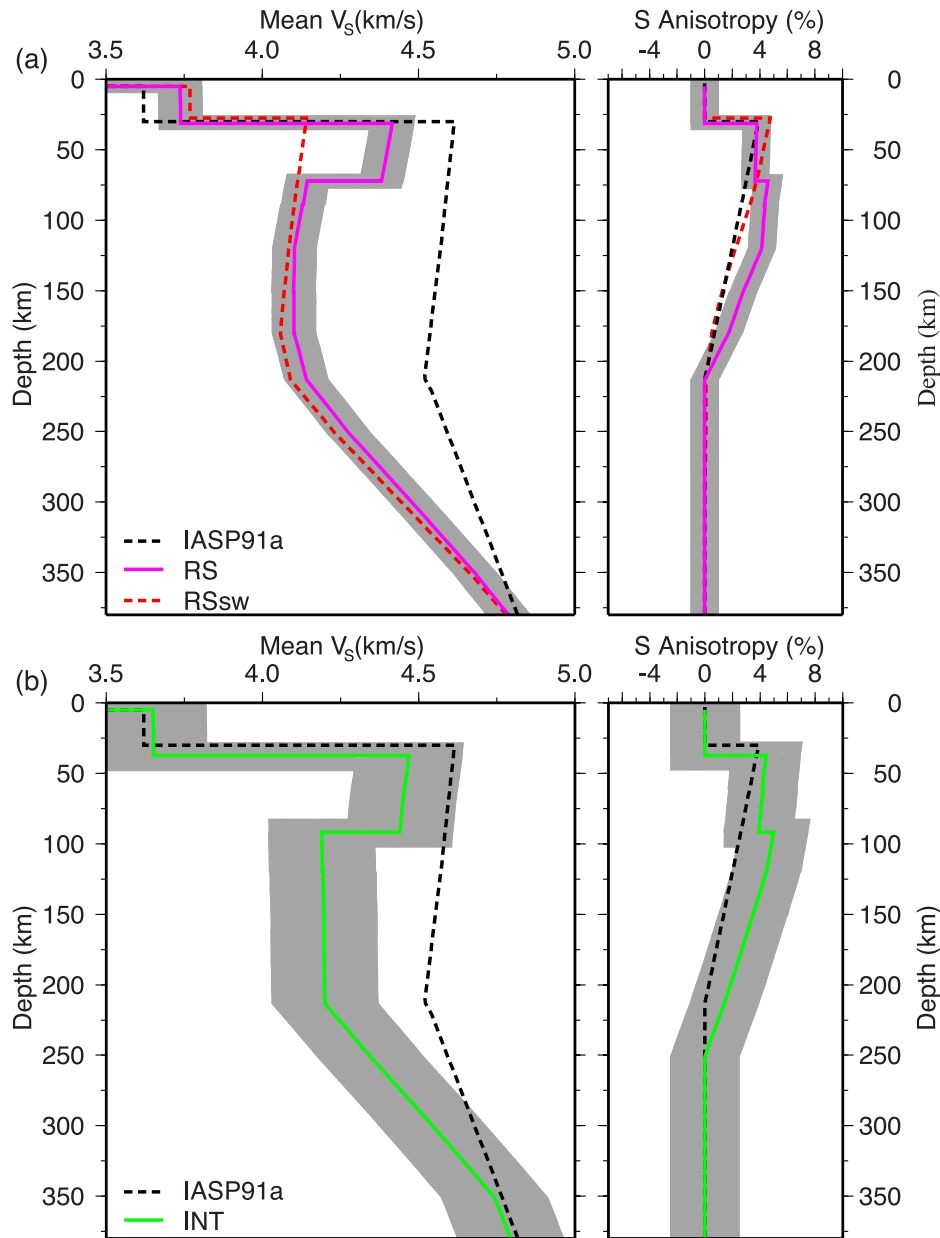


Figure 9. Radially anisotropic shear velocity models of upper-mantle structure beneath (a) the Red Sea transect (RS) and beneath (b) the interior transect (INT), derived from inversion of surface wave delays and receiver function constraints. The gray shaded areas show the associated uncertainties reported in the text; however, quantification of the base of the LVZ also suggests that resolution below ~ 210 km is poor. Also shown in (a) is model RSsw (red dashed curves), which is the preferred subarray model for the Red Sea transect obtained by only using the surface wave delay times (without including the receiver function S-P constraints in the inversion). In both (a) and (b), the left panel displays mean shear velocity ($V_S = (V_{SH} + V_{SV})/2$), while the right panel displays shear anisotropy ($\Delta V_S = (V_{SH} - V_{SV})/V_S$ in percent). Reference model IASP91a is shown by the black dashed curves.

to within about ± 0.07 km/s and shear anisotropy is resolved to within about ± 1 percent. The estimated error for the reported Moho and LAB depths is ± 5 km. For the interior transect, uncertainties associated with the path model and limited data availability lead to errors that are about 2 to 2.5 times larger than those associated with the Red Sea transect. Additionally, the minimum depth of the base of the

LVZ along the Red Sea transect was quantified by forcing the RS model (Figure 9) to return to IASP91a at different depths. Models with faster, IASP91a-comparable velocities at and above 180 km resulted in notable misfits to the low frequency Rayleigh wave data (Figures 4–5). Therefore the LVZ must extend to depths greater than 180 km. On the basis of this assessment, the LVZ could terminate as

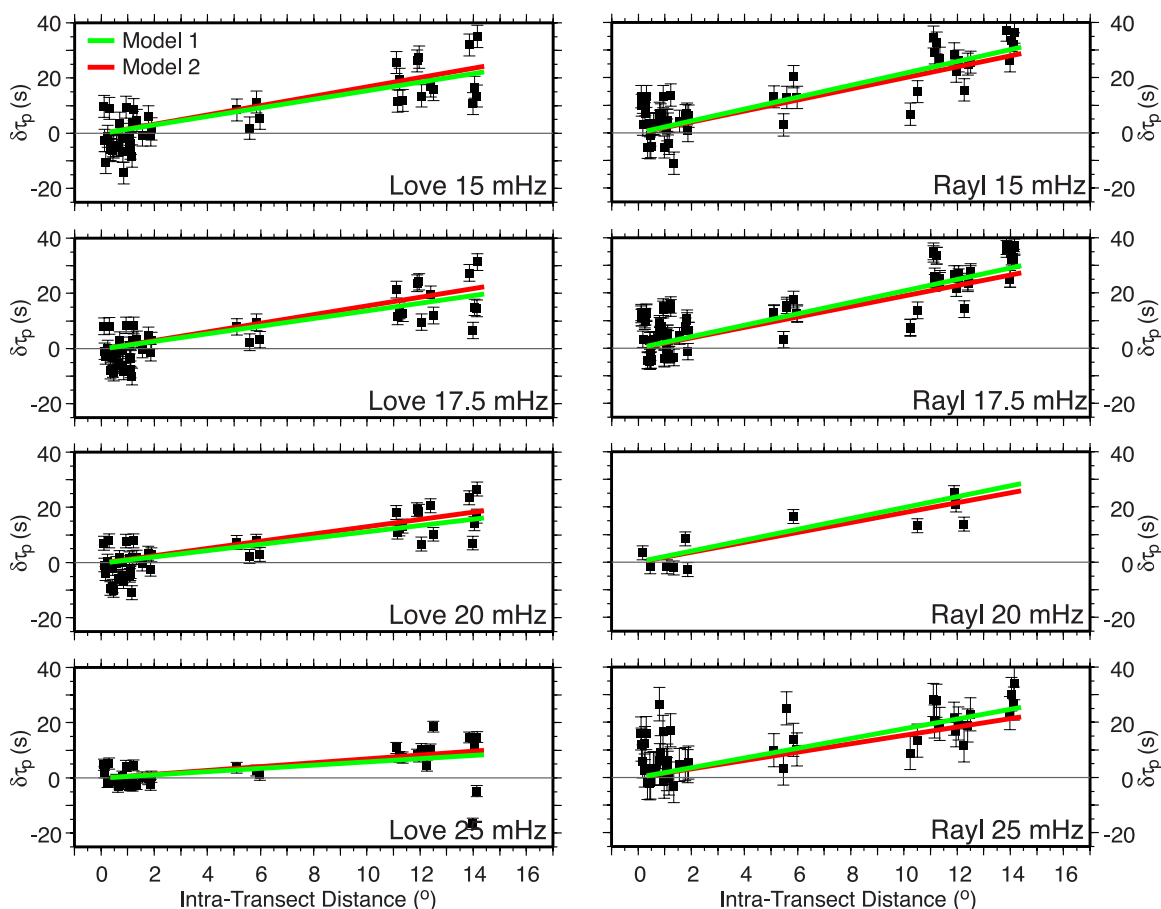


Figure 10. Evaluation of azimuthally anisotropic models constructed from shear-wave splitting results of *Hansen et al.* [2006], using the phase-delay behavior for Love (left panels) and Rayleigh (right panels) waves at frequencies most sensitive to structure between the Moho and 200-km depth (15–25 mHz). Solid symbols represent surface wave observations along the Red Sea transect, corrected for structure outside the array and referenced to the isotropic average of RS. Curves represent predicted phase delays for the two different elastic structures in Table 1 (model 1: green curve, model 2: red curve).

shallowly as 210 km; however, given the flexibility, the inversion maintains low velocities down to about 250 km.

4. Forward Models of Azimuthal Anisotropy

[25] Shear wave splitting results from *Hansen et al.* [2006] provide estimates of azimuthal anisotropy throughout Arabia (Figure 1). This anisotropy most likely arises from the lattice preferred orientation in peridotite rocks, where ϕ corresponds to the olivine crystallographic a -axes [100] and the δt represents the shear velocity difference integrated over depth [e.g., *Silver*, 1996]. Assuming that the peridotite elasticity in Arabia is comparable to that observed in ophiolite outcrops and xenolith samples, the average δt of 1.4 s implies an anisotropic layer 100–350 km thick. The lower thickness estimate corresponds to strong anisotropy ($\sim 6\%$), like that observed in oceanic environments and ridge peridotites [*Kawasaki and Kon'no*, 1984; *Ben-Ismaïl and Mainprice*, 1998]. If the anisotropy is weaker ($\sim 2\%$), such as that observed in xenoliths from continental cratons [*Peselnick and Nicolas*, 1978; *Ben-Ismaïl et al.*, 2001], a thicker layer is necessary. These constraints provide end-member models which are considered in this section.

[26] The goal is to find an average 1D azimuthally anisotropic model that satisfies both the shear wave splitting observations from the SANDSN stations as well as the observed surface wave delay times. Models with different distributions of anisotropy were developed using the average ϕ from the examined transects to specify the orientation of the local elasticity tensor. Layer thicknesses and elastic parameters were combined such that the resulting models produced the average 1.4 s δt observed. Using the surface wave partial derivative kernels and first-order perturbation theory [*Montagner and Nataf*, 1986], the azimuthally anisotropic models were evaluated by calculating their predicted phase delay behavior for Love and Rayleigh waves propagating along the examined transects.

[27] Figures 10 and 11 display the path-corrected surface-wave phase delays at several frequencies along the Red Sea and interior transects, respectively, along with the predicted phase delay behavior of two azimuthally anisotropic models (Table 1). The angle between ϕ and the propagation direction is large enough that the $V_{SH} > V_{SV}$ behavior is clear [*Maupin*, 1985], and the model predictions match the data well. While many different distributions of azimuthal anisotropy are able to fit the trends equally well, the

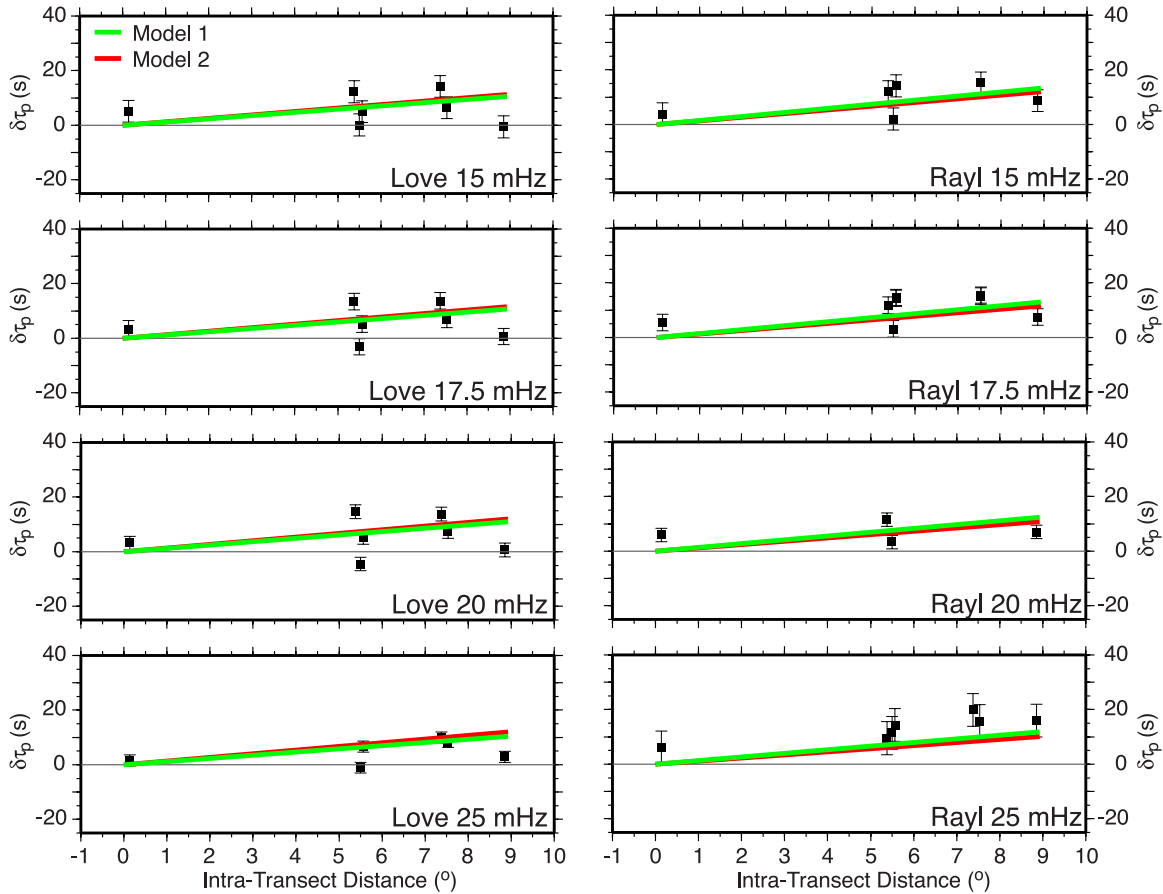


Figure 11. Same as Figure 10, but now the solid symbols represent surface wave observations along the interior transect, corrected for structure outside the array and referenced to the isotropic average of INT.

inversion results (RS and INT) illustrate the importance of anisotropy in both the lithosphere and asthenosphere. Therefore we favor the azimuthally anisotropic models that had both a lithospheric and asthenospheric contribution (Table 1 and Figures 10 and 11).

5. Discussion

5.1. Shear Velocities

[28] Our velocity models (Figure 9) illustrate that the LAB beneath Arabia is associated with a dramatic V_S decrease in the asthenosphere, required to fit the positive phase delay observations and LAB S-P times (Figures 4–7). The minimum V_S ranges from about 4.1 km/s near the Red Sea to about 4.2 km/s in the Arabian interior. *Tkalčić et al.* [2006], who jointly inverted surface wave group velocities and P wave receiver

functions, found minimum V_S of about 4.0 km/s near the Red Sea and 4.3 km/s in the interior, agreeing well with the velocities inferred in this study. Modeling of S-wave receiver functions found similar sub-LAB velocities, averaging about 4.2 km/s [*Hansen et al.*, 2007]. Figure 12 compares the preferred Red Sea model (RS, Figure 9) from this study to one-dimensional profiles extracted from both the regional surface wave tomography model of *Park et al.* [2008] as well as the global CU Boulder model CU_SRT1.0 [*Barmin et al.*, 2001]. Differences in model parameterization and choice of data make this comparison difficult. The corridor approach chosen for the RS model averages the structure along the Red Sea in a single 1D layered framework, but it specifically incorporates data that can provide localized sampling in a narrow zone along the margin. The tomographic models provide smooth 3D varia-

Table 1. Azimuthally Anisotropic Forward Models

Model	Transect	Layer Depths (km)	ΔV_S (%) ^a	Reference
Model 1	RS (Figure 10)	31–266	2.6	<i>Ben-Ismaïl and Mainprice</i> [1998]
Model 2	RS (Figure 10)	31–128	6.4	<i>Ben-Ismaïl et al.</i> [2001]
Model 1	INT (Figure 11)	37–247	2.6	<i>Ben-Ismaïl and Mainprice</i> [1998]
Model 2	INT (Figure 11)	37–124	6.4	<i>Ben-Ismaïl et al.</i> [2001]

^aPercentage difference in the velocities of two vertically propagating shear waves in the anisotropic layer. All models are constructed to produce 1.4 s of total splitting.

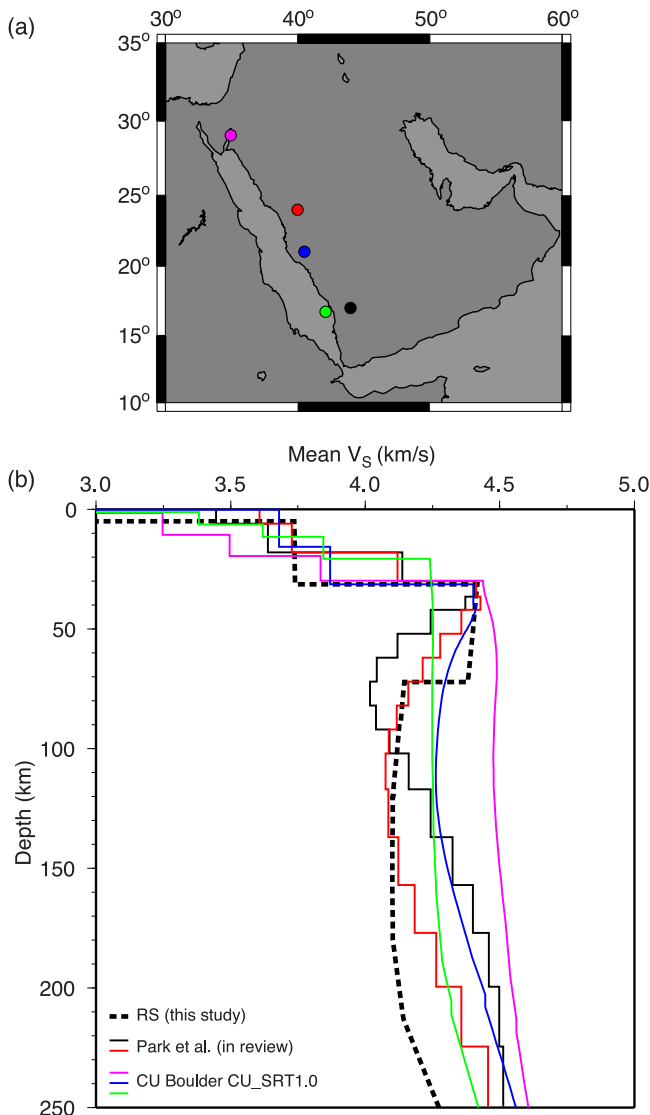


Figure 12. Comparison of the Red Sea upper-mantle shear velocity model from this study with one-dimensional velocity profiles extracted from both the regional surface wave tomography model of *Park et al.* [2008] and the global CU Boulder CU_SRT1.0 model [*Barmin et al.*, 2001]. (a) Locations along the Red Sea where one-dimensional profiles were extracted. (b) Comparison of mean shear velocity ($V_S = (V_{SH} + V_{SV})/2$) versus depth. For the extracted profiles, the color of the location marker in (a) matches the color of the profile in (b) (red, black: *Park et al.* [2008]; green, blue, pink: *Barmin et al.* [2001]). The preferred Red Sea model (RS) from this study is shown by the black dashed line.

tions, but with different spatial gridding: $2 \times 2^\circ$ for the CU Boulder model and 50×50 km for the regional model. Despite these differences, all three models clearly show that the Red Sea region is quite slow through the upper mantle compared to global average models such as IASP91. *Park et al.* [2008] report a broad, low-velocity region extending to a depth of

150 km everywhere beneath the Arabian Shield with a narrower low-velocity region along the Red Sea extending to depths greater than 150 km. This agrees very well with our findings. The CU_SRT1.0 model does not resolve the lithosphere-asthenosphere transition, but the average upper-mantle velocities show a distinct trend from north to south that suggests very slow velocities in the southern Red Sea region. The RS model is consistently slower than the other models below ~ 120 km depth. As discussed previously, the quantification of the base of the LVZ suggests that these velocities are robust to at least 180 km depth.

[29] Other continental rift environments also display low velocities similar to those observed in this study. Beneath the western Antarctic and Baikal rifts, V_S in the LVZ reaches a minimum of about 4.2 km/s [*Ritzwoller et al.*, 2001; *Yanovskaya and Kozhevnikov*, 2003]. In the Gulf of California, a pronounced LVZ is inferred at about 70 km depth with V_S up to 10% slower than the global AK135 reference model [*Zhang et al.*, 2007, Figure 13]. *Weeraratne et al.* [2003] examined velocities beneath the east and west branches of the East African Rift in Tanzania and found a LVZ starting around 75 km depth, with the slowest velocities between 100–160 km. The minimum velocities are 12–20% slower than the Tanzanian craton, averaging about 3.9 km/s (Figure 13). However, it should be noted that decreased raypath coverage reduced the resolution in the rifts, and *Weeraratne et al.* [2003] suggest that a 7–8% velocity contrast is more reasonable. Back-arc spreading centers, such as that beneath north Fiji and Lau, also display very low seismic velocities, with V_S as slow as 3.8 km/s [*Xu and Wiens*, 1997]. Similar low velocities to those inferred in this study are also seen in oceanic ridge environments. Relatively young seafloor along the East Pacific Rise is underlain by low V_S (0–4 Ma: $V_S = 4.0$ km/s, 4–20 Ma: $V_S = 4.2$ km/s [*Nishimura and Forsyth*, 1989, Figure 13]) similar to that observed near the Red Sea. The minimum V_S observe in our study is also similar to the V_S found below 6–10 Ma seafloor in the Kolbeinsey and south Azores segments and 4–6 Ma seafloor in the south Ascension and Reykjanes segments of the mid-Atlantic ridge [*Gaherty and Dunn*, 2007, Figure 13].

[30] It has been suggested that channelized flow from the Afar hot spot may be responsible for the low velocities observed beneath western Arabia and the Red Sea [*Camp and Roobol*, 1992; *Ebinger and Sleep*, 1998; *Hansen et al.*, 2006, 2007]. The LVZ in our study extends to a depth of about 180 km, much deeper than the LVZ seen in other continental rift and oceanic ridge environments (Figure 13). Despite the data scatter, low shear velocities at depth are required to fit the strong positive trends in the lowest frequency phase delays (Figures 4–5). The depth extent of the LVZ may be a signature of the hot spot’s influence. As the asthenosphere is fed by hot material from the Afar upwelling, that hot, buoyant material spreading northward may become trapped by lithospheric topography and surrounding tectonic boundaries. With only recent, slow spreading along the Red Sea Rift to efficiently cool this material, it may pond at the base of the lithosphere to form a “thick” asthenospheric layer. Such a “plume-fed” asthenosphere has been proposed by *Phippis Morgan et al.* [1995] as a mechanism to produce hot, weak asthenospheric mantle

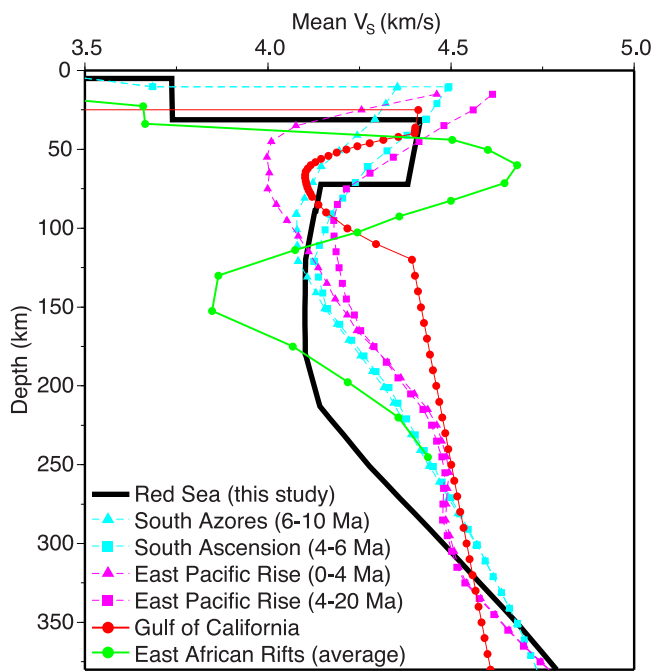


Figure 13. Comparison of the Red Sea upper-mantle shear velocity model (RS, bold black curve) developed in this study with velocity models from other continental rift and oceanic ridge environments. Blue dashed curves: south Azores (6–10 Ma, triangles) and south Ascension (4–6 Ma, squares) sections of the mid-Atlantic ridge [Gaherty and Dunn, 2007]; Pink dashed curves: 0–4 Ma (triangles) and 4–20 Ma (squares) seafloor along the East Pacific Rise [Nishimura and Forsyth, 1989]; Red circles: Gulf of California [Zhang et al., 2007]; Green circles: average velocities from the east and west branches of the East African Rift [Weeraratne et al., 2003].

beneath the ocean basins on a global scale; our observation may provide support for this process on a regional scale.

[31] The presence of hot material associated with the Afar upwelling could also lead to some degree of partial melt beneath the Arabian Shield and the Red Sea, which would significantly lower the asthenospheric shear velocity and result in a high velocity contrast across the LAB, such as that observed here. Some recent studies [Faul and Jackson, 2005; Priestley and McKenzie, 2006] have argued that the increase in temperature with depth alone is sufficient to explain observed LVZs and that melt is not required. To obtain V_S as low as those observed beneath Arabia, these models require very high attenuation (low Q) in the asthenosphere [e.g., Yang et al., 2007]. Little to no constraints on Q beneath Arabia are currently available, and while this will be explored in future work, it is beyond the scope of this study. Therefore we cannot conclusively determine if partial melt is present beneath western Arabia and the Red Sea, but the sharp velocity contrast across the LAB and the depth extent of the low V_S observed suggest that the presence of partial melt is not unreasonable.

5.2. Seismic Anisotropy

[32] The subarray inversion models (RS and INT) display an average 4.0% anisotropy in the lithosphere, increasing to an average 4.8% anisotropy across the LAB. Generally,

these percentages of anisotropy are similar to those observed for 5–10 Ma seafloor in the Ascension and Azores segments of the mid-Atlantic Ridge [Gaherty and Dunn, 2007]. The change in anisotropy across the LAB is at the limit of our resolution (Figure 9), so care must be taken in the interpretation of this feature. However, similar increases in anisotropy at the base of the lithosphere have been observed in a number of oceanic [Gaherty et al., 1996; Plomerová et al., 2002] and continental [Plomerová et al., 2002] environments. The LAB is widely recognized as a mechanical and thermal boundary [e.g., Jordan, 1978, 1988; Poudjom Djomani et al., 2001] and has also been associated with an increase in electrical conductivity [Jones, 1999]. It is possible that the LAB may also be associated with a distinct change in seismic anisotropy [Plomerová et al., 2002].

[33] Forward models of azimuthal anisotropy, based on shear wave splitting, also satisfy the surface wave delay times. Models with anisotropy in both the lithosphere and asthenosphere are favored since the inversion results required contributions from both of these regions. In these models, ϕ in both layers is the same since examination of the shear wave splitting found no evidence for multiple anisotropic layers [Hansen et al., 2006]. Given the fairly good back-azimuth coverage of the shear wave splitting observations, this is an adequate approximation. The lithosphere, especially near the Red Sea coast, is not thick enough to generate the observed δt , but a lithospheric component cannot be completely ruled out by the splitting since the terranes composing the Arabian Shield may contain fossilized anisotropy with a similar north-south oriented ϕ . If anisotropy is present in the lithosphere (as the surface wave data indicate), the thin lid makes any splitting contribution from this anisotropy small compared to that generated in the underlying asthenosphere. Therefore we believe that our anisotropic signature is dominated by anisotropy in the asthenosphere and is consistent with the interpretation of Hansen et al. [2006] that this anisotropy reflects a combination of plate- and density-driven flow associated with rifting processes in the Red Sea.

[34] In many environments, the anisotropic models derived from surface wave data are inconsistent with observed shear wave splitting [e.g., Montagner et al., 2000; Freybourger et al., 2001; Gaherty, 2004; Debayle et al., 2005]. These studies, which examine continental cratons, must explain their observations with two very different layers of anisotropy: a shallow lithospheric layer that generates the Love-Rayleigh wave discrepancy and a deeper asthenospheric layer that generates the shear wave splitting. Even when surface and body wave observations are simultaneously inverted [Marone and Romanowicz, 2007], multiple anisotropic layers with different elastic properties are required to explain the anisotropy observed in cratonic regions. This is because surface and body waves do not “see” the same structure; their depths of sampling are quite different [e.g., Marone and Romanowicz, 2007] and they average small-scale structural heterogeneity in very different ways [e.g., Saltzer et al., 2000; Gaherty, 2004]. However, in tectonically active regions, like the western United States and central Asia, where large-scale tectonic processes are occurring, there is generally good agreement between the surface- and body wave anisotropy [Montagner et al., 2000; Davis, 2003; Yang and Forsyth, 2006; Marone and

Romanowicz, 2007]. Such agreement should only be expected in areas where there is limited lithospheric variation and large-scale shear wave splitting consistency [Montagner et al., 2000]. The Red Sea and central Arabian Shield meet this requirement as there is little contribution from the thin lithosphere to the observed shear wave splitting and the anisotropic signature is dominated by the asthenospheric component. Therefore in this region we are able to reconcile the body and surface wave anisotropy observations.

6. Conclusions

[35] We investigated the lithospheric and upper mantle shear-velocity structure and the depth-dependence of anisotropy along the Red Sea and beneath the Arabian Peninsula by modeling surface wave phase velocities and receiver function constraints along two transects of the SANDSN. The lithosphere, which ranges in thickness from about 70 km near the Red Sea coast to about 90 km beneath the Arabian Shield, is underlain by a pronounced LVZ with V_S as low as 4.1 km/s. Similar low V_S values have been observed in other continental rifts as well as oceanic ridge environments and back-arc spreading centers, but the LVZ in this study extends to much greater depth than the LVZs seen in other environments. The depth extent of the low V_S and sharp velocity contrast across the LAB may indicate the influence of the Afar hot spot and the presence of partial melt. Radially anisotropic models require both lithospheric and asthenospheric anisotropy to fit the observed surface wave delays. Shear wave splitting observations and surface wave delay times can be reconciled by azimuthally anisotropic models, which are dominated by anisotropy in the asthenosphere resulting from plate- and density-drive flow associated with rifting in the Red Sea.

[36] **Acknowledgments.** We thank Thorne Lay, Hanneke Paulssen, and Keith Priestley for their helpful discussions as well as Michael Ritzwoller and two anonymous reviewers for their thorough critiques of this manuscript. Figures were prepared using GMT [Wessel and Smith, 1998]. Support for this work was provided by CSIDE/IGPP and the LLNL Student Employee Graduate Research Fellow program. This work was performed under the auspices of the U.S. Department of Energy by University of California, Lawrence Livermore National Laboratory under contract W-7405-Eng-48. This is LLNL contribution UCRL-JRNL-233119.

References

- Al-Amri, M., and A. Al-Amri (1999), Configuration of the seismographic networks in Saudi Arabia, *Seismol. Res. Lett.*, *70*, 322–331.
- Al-Damegh, K., E. Sandvol, and M. Barazangi (2005), Crustal structure of the Arabian Plate: New constraints from the analysis of teleseismic receiver functions, *Earth Planet. Sci. Lett.*, *231*, 177–196.
- Barmin, M., M. Ritzwoller, and A. Levshin (2001), A fast and reliable method for surface wave tomography, *PAGEOPH*, *158*, 1351–1375.
- Ben-Ismaïl, W., and D. Mainprice (1998), An olivine fabric database: An overview of upper mantle fabrics and seismic anisotropy, *Tectonophysics*, *296*, 145–157.
- Ben-Ismaïl, W., G. Barruol, and D. Mainprice (2001), The Kaapvaal craton seismic anisotropy: Petrophysical analyses of upper mantle kimberlite nodules, *Geophys. Res. Lett.*, *28*, 2497–2500.
- Benoit, M., A. Nyblade, J. Vandecar, and H. Gurrola (2003), Upper mantle P wave velocity structure and transition zone thickness beneath the Arabian Shield, *Geophys. Res. Lett.*, *30*(10), 1531, doi:10.1029/2002GL016436.
- Camp, V., and M. Roobol (1992), Upwelling asthenosphere beneath western Arabia and its regional implications, *J. Geophys. Res.*, *97*, 15,255–15,271.
- Daradich, A., J. Mitrovica, R. Pysklywec, S. Willett, and A. Forte (2003), Mantle flow, dynamic topography, and rift-flank uplift of Arabia, *Geology*, *31*, 901–904.
- Davis, P. (2003), Azimuthal variation in seismic anisotropy of the southern California uppermost mantle, *J. Geophys. Res.*, *108*(B1), 2052, doi:10.1029/2001JB000637.
- Debayle, E., J. Lévêque, and M. Cara (2001), Seismic evidence for a deeply rooted low-velocity anomaly in the upper mantle beneath the northeastern Afro-Arabian continent, *Earth Planet. Sci. Lett.*, *193*, 423–436.
- Debayle, E., B. Kennett, and K. Priestley (2005), Global azimuthal seismic anisotropy and the unique plate-motion deformation of Australia, *Nature*, *433*, 509–512.
- Di Luccio, F., and M. Pasyanos (2007), Crustal and upper-mantle structure in the Eastern Mediterranean from the analysis of surface wave dispersion curves, *Geophys. J. Int.*, *169*, 1139–1152.
- Dziewonski, A., and D. Anderson (1981), Preliminary reference Earth model, *Phys. Earth Planet. Inter.*, *25*, 297–356.
- Ebinger, C., and N. Sleep (1998), Cenozoic magmatism throughout east Africa resulting from impact of a single plume, *Nature*, *395*, 788–791.
- Faul, U., and I. Jackson (2005), The seismological signature of temperature and grain size variations in the upper mantle, *Earth Planet. Sci. Lett.*, *234*, 119–134.
- Freybourger, M., J. Gaherty, and T. Jordan (2001), and the Kaapvaal Seismic Group, Structure of the Kaapvaal craton from surface waves, *Geophys. Res. Lett.*, *28*, 2489–2492.
- Gaherty, J. (2004), A surface wave analysis of seismic anisotropy beneath eastern North America, *Geophys. J. Int.*, *158*, 1053–1066.
- Gaherty, J., and R. Dunn (2007), Evaluating hot spot-ridge interaction in the Atlantic from regional-scale seismic observations, *Geochem. Geophys. Geosyst.*, *8*, Q05006, doi:10.1029/2006GC001533.
- Gaherty, J., and T. Jordan (1995), Lehmann discontinuity as the base of an anisotropic layer beneath continents, *Science*, *268*, 1468–1471.
- Gaherty, J., T. Jordan, and L. Gee (1996), Seismic structure of the upper mantle in a central Pacific corridor, *J. Geophys. Res.*, *101*, 22,291–22,309.
- Gaherty, J., M. Kato, and T. Jordan (1999), Seismological structure of the upper mantle: A regional comparison of seismic layering, *Phys. Earth Planet. Inter.*, *110*, 21–41.
- Gee, L., and T. Jordan (1992), Generalized seismological data functionals, *Geophys. J. Int.*, *111*, 363–390.
- Gök, R., E. Sandvol, N. Türkelli, D. Seber, and M. Barazangi (2003), Sn attenuation in the Anatolian and Iranian plateau and surrounding regions, *Geophys. Res. Lett.*, *30*(24), 8042, doi:10.1029/2003GL018020.
- Gök, R., M. Pasyanos, and E. Zor (2007), Lithospheric structure of the continent-continent collision zone: Eastern Turkey, *Geophys. J. Int.*, *169*, 1079–1088.
- Hansen, S., S. Schwartz, A. Al-Amri, and A. Rodgers (2006), Combined plate motion and density driven flow in the asthenosphere beneath Saudi Arabia: Evidence from shear-wave splitting and seismic anisotropy, *Geology*, *34*, 869–872.
- Hansen, S., A. Rodgers, S. Schwartz, and A. Al-Amri (2007), Imaging ruptured lithosphere beneath the Red Sea and Arabian Peninsula, *Earth Planet. Sci. Lett.*, *259*, 256–265.
- Jones, A. (1999), Imaging the continental upper mantle using electromagnetic methods, *Lithos*, *48*, 57–80.
- Jordan, T. (1978), Composition and development of the continental tectosphere, *Nature*, *274*, 544–548.
- Jordan, T. (1988), Structure and formation of the continental tectosphere, *J. Petrol.*, 11–37, (Special Lithosphere issue).
- Julià, J., C. Ammon, and R. Herrmann (2003), Lithospheric structure of the Arabian Shield from the joint inversion of receiver functions and surface-wave group velocities, *Tectonophysics*, *371*, 1–12.
- Kawasaki, I., and F. Kon'no (1984), Azimuthal anisotropy of surface waves and the possible type of the seismic anisotropy due to preferred orientation of olivine in the uppermost mantle beneath the Pacific Ocean, *J. Phys. Earth*, *32*, 229–244.
- Kennett, B., and E. Engdahl (1991), Traveltimes for global earthquake location and phase identification, *Geophys. J. Int.*, *105*, 429–465.
- Marone, F., and B. Romanowicz (2007), The depth distribution of azimuthal anisotropy in the continental upper mantle, *Nature*, *447*, 198–203.
- Maupin, V. (1985), Partial derivatives of surface-wave phase velocities for flat anisotropic models, *Geophys. J. R. Astron. Soc.*, *83*, 379–398.
- McGuire, A., and R. Bohannon (1989), Timing of mantle upwelling: Evidence for a passive origin for the Red Sea Rift, *J. Geophys. Res.*, *94*, 1677–1682.
- Montagner, J.-P., and H. Nataf (1986), A simple method for inverting the azimuthal anisotropy of surface waves, *J. Geophys. Res.*, *91*, 511–520.
- Montagner, J.-P., D. Griot-Pommeroy, and J. Lavé (2000), How to relate body wave and surface wave anisotropy?, *J. Geophys. Res.*, *105*, 19,015–19,027.
- Nishimura, C., and D. Forsyth (1989), The anisotropic structure of the upper mantle in the Pacific, *Geophys. J.*, *96*, 203–229.

- Nyblade, A., Y. Park, A. Rodgers, and A. Al-Amri (2006), Seismic structure of the Arabian Shield Lithosphere and Red Sea Margin, *Margins Newslett.*, *17*, 13–15.
- Park, Y., A. Nyblade, A. Rodgers, and A. Al-Amri (2007), Upper mantle structure beneath the Arabian Peninsula from regional body wave tomography: Implications for the origin of Cenozoic uplift and volcanism in the Arabian Shield, *Geochem. Geophys. Geosyst.*, *8*, Q06021, doi:10.1029/2006GC001566.
- Park, Y., A. A. Nyblade, A. J. Rodgers, and A. Al-Amri (2008), S wave velocity structure of the Arabian Shield upper mantle from Rayleigh wave tomography, *Geochem. Geophys. Geosyst.*, *9*, Q07020, doi:10.1029/2007GC001895.
- Peselnick, L., and A. Nicolas (1978), Seismic anisotropy in an ophiolite peridotite: Application to oceanic upper mantle, *J. Geophys. Res.*, *83*, 1227–1235.
- Phipps Morgan, J., W. J. Morgan, Y. Zhang, and W. Smith (1995), Observational hints for a plume-fed, suboceanic asthenosphere and its role in mantle convection, *J. Geophys. Res.*, *100*, 12,753–12,767.
- Plomerová, J., K. Daniel, and V. Babuška (2002), Mapping the lithosphere-asthenosphere boundary through changes in surface-wave anisotropy, *Tectonophysics*, *358*, 175–185.
- Poudjom Djomani, Y., S. O'Reilly, W. Griffin, and P. Morgan (2001), The density structure of subcontinental lithosphere through time, *Earth Planet. Sci. Lett.*, *184*, 605–621.
- Priestley, K., and D. McKenzie (2006), The thermal structure of the lithosphere from shear wave velocities, *Earth Planet. Sci. Lett.*, *244*, 285–301.
- Ritzwoller, M., N. Shapiro, A. Levshin, and G. Leahy (2001), Crustal and upper mantle structure beneath Antarctica and surrounding oceans, *J. Geophys. Res.*, *106*, 30,645–30,670.
- Rodgers, A., W. Walter, R. Mellors, A. Al-Amri, and Y. Zhang (1999), Lithospheric structure of the Arabian Shield and Platform from complete regional waveform modeling and surface wave group velocities, *Geophys. J. Int.*, *138*, 871–878.
- Saltzer, R., J. Gaherty, and T. Jordan (2000), How are vertical shear wave splitting measurements affected by variations in the orientation of azimuthal anisotropy with depth?, *Geophys. J. Int.*, *141*, 374–390.
- Sandvol, E., D. Seber, M. Barazangi, F. Vernon, R. Mellors, and A. Al-Amri (1998), Lithospheric seismic velocity discontinuities beneath the Arabian Shield, *Geophys. Res. Lett.*, *25*, 2873–2876.
- Silver, P. (1996), Seismic anisotropy beneath the continents: Probing the depths of Geology, *Ann. Rev. Earth Planet. Sci.*, *24*, 385–432.
- Stoeser, D., and V. Camp (1985), Pan-African microplate accretion of the Arabian Shield, *GSA Bull.*, *96*, 817–826.
- Tkalčić, H., M. Pasyanos, A. Rodgers, R. Gök, W. Walter, and A. Al-Amri (2006), A multistep approach for joint modeling of surface wave dispersion and teleseismic receiver functions: Implications for lithospheric structure of the Arabian Peninsula, *J. Geophys. Res.*, *111*, B11311, doi:10.1029/2005JB004130.
- Voggenreiter, W., H. Hötzl, and A. Jado (1988), Red Sea related history of extension and magmatism in the Jizan area (southwest Saudi Arabia): Indication for simple-shear during Red Sea rifting, *Geol. Rundsch.*, *77*, 257–274.
- Weeraratne, D., D. Forsyth, K. Fischer, and A. Nyblade (2003), Evidence for an upper mantle plume beneath the Tanzanian craton from Rayleigh wave tomography, *J. Geophys. Res.*, *108*(B9), 2427, doi:10.1029/2002JB002273.
- Wernicke, B. (1985), Uniform-sense normal simple-shear of the continental lithosphere, *Can. J. Earth Sci.*, *22*, 108–125.
- Wessel, P., and W. Smith (1998), New, improved version of the Generic Mapping Tools released, *Eos Trans. AGU*, *79*, 579.
- Wolfe, C., F. Vernon, and A. Al-Amri (1999), Shear-wave splitting across western Saudi Arabia: The pattern of upper mantle anisotropy at a Proterozoic shield, *Geophys. Res. Lett.*, *26*, 779–782.
- Xu, Y., and D. Wiens (1997), Upper mantle structure of the southwest Pacific from regional waveform inversion, *J. Geophys. Res.*, *102*, 27,439–27,451.
- Yang, Y., and D. Forsyth (2006), Rayleigh wave phase velocities, small-scale convection, and azimuthal anisotropy beneath southern California, *J. Geophys. Res.*, *111*, B07306, doi:10.1029/2005JB004180.
- Yang, Y., D. Forsyth, and D. Weeraratne (2007), Seismic attenuation near the East Pacific Rise and the origin of the low-velocity zone, *Earth Planet. Sci. Lett.*, *258*, 260–268.
- Yanovskaya, T., and V. Kozhevnikov (2003), 3D S-wave velocity pattern in the upper mantle beneath the continent of Asia from Rayleigh wave data, *Phys. Earth Planet. Inter.*, *138*, 263–278.
- Zhang, X., H. Paulssen, S. Lebedev, and T. Meier (2007), Surface wave tomography of the Gulf of California, *Geophys. Res. Lett.*, *34*, L15305, doi:10.1029/2007GL030631.

A. M. S. Al-Amri, Geology Department and Seismic Studies Center, King Saud University, P.O. Box 2455, Riyadh 11451, Saudi Arabia.

J. B. Gaherty, Lamont-Doherty Earth Observatory, Columbia University, P.O. Box 1000, 61 Route 9W, Palisades, NY 10964, USA.

S. E. Hansen, Geosciences Department, Pennsylvania State University, 407 Deike Building, University Park, PA 16802, USA. (shansen@geosc.psu.edu)

A. J. Rodgers, Energy and Environment Directorate, Lawrence Livermore National Laboratory, 7000 East Avenue, Livermore, CA 94551, USA.

S. Y. Schwartz, Earth and Planetary Sciences Department, University of California, Santa Cruz, 1156 High Street, Santa Cruz, CA 95064, USA.